Supplementary Information

Thermal Rectification of Shape Memory Polymer Composites by Programmable Conductivity Modulation

Seongkyun Kim et al.

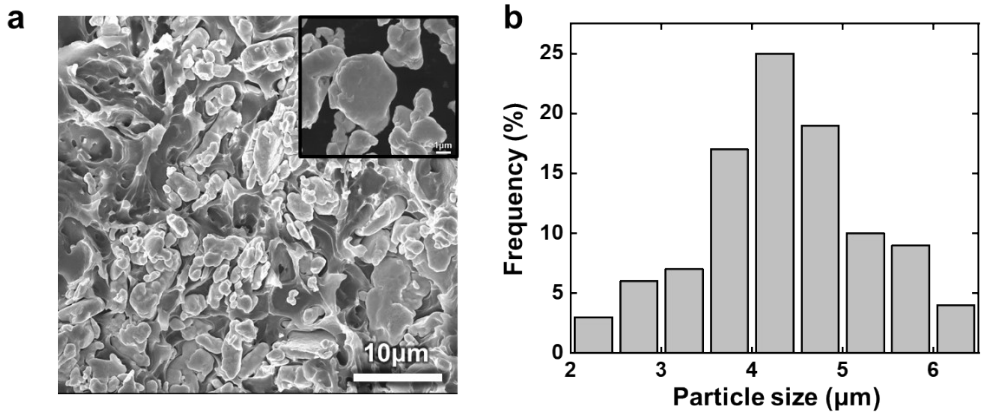

Supplementary Fig. 1 The dispersion and size analysis of the AgFLs. a SEM image of the SMPC. **b** The size distribution of the AgFLs.

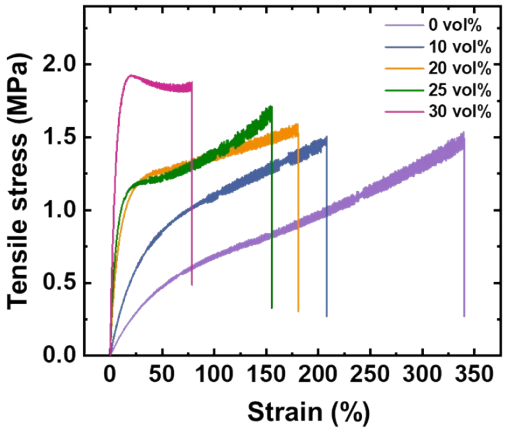

Supplementary Fig. 2 The strain-stress characteristics of the SMPC (AgFL = 0-30 vol%).

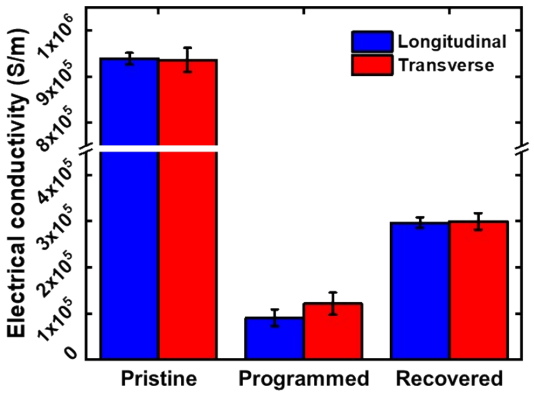

Supplementary Fig. 3 The electrical conductivity of the pristine, programmed, and recovered SMPCs. The σ is measured by the four-point probe in-line method. The error bar represents the standard deviation of the data.

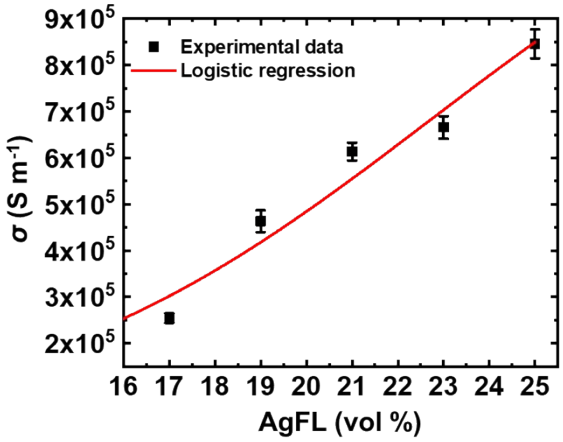

Supplementary Fig. 4 The electrical conductivity of the SMPC as a function of AgFL concentration. The data are fitted to a logistic regression model, and the regression error (R^2) is 0.9604.[1]

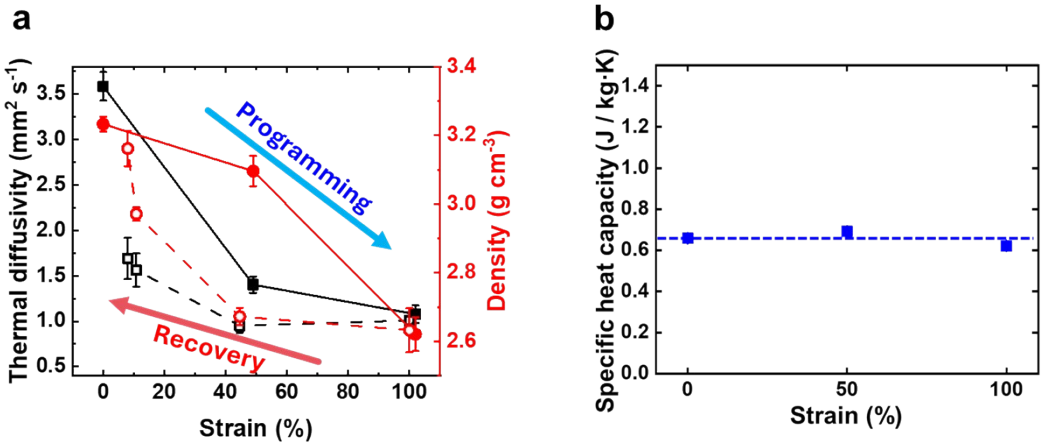

Supplementary Fig. 5 The thermal diffusivity, density, and specific heat capacity of the SMPC are shown as a function of strain. a The thermal diffusivity and density are shown as a function of strain during the first programming-recovery cycle. The solid and open symbols represent the data during the programming and recovery processes, respectively. **b** The specific heat capacity is shown as a function of strain.

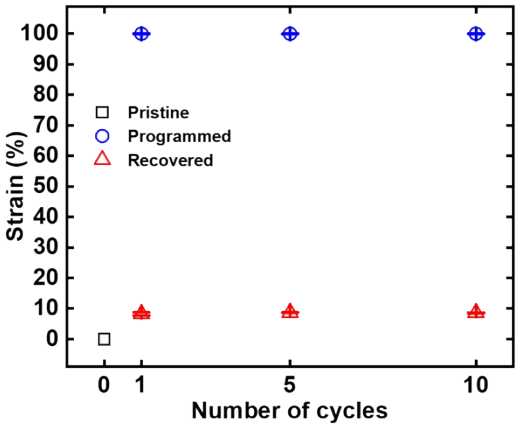

Supplementary Fig. 6 The strain modulation as a function of the number of programming-recovery cycles. The error bar represents the standard deviation of the data.

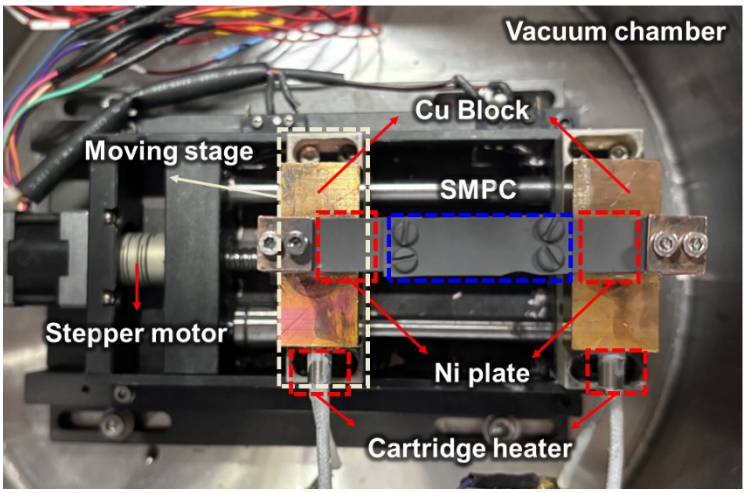

Supplementary Fig. 7 The optical image of the thermal rectification experimental setup.

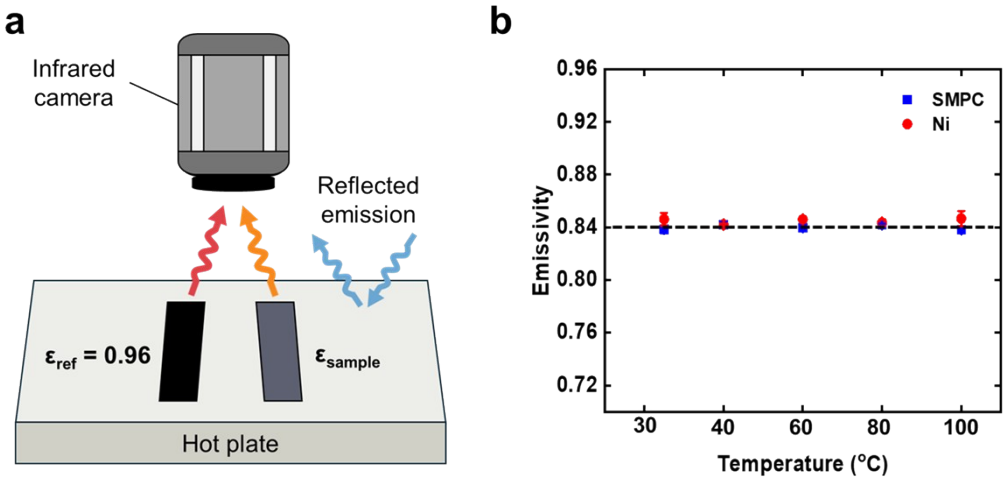

Supplementary Fig. 8 The reflected temperature and emissivity are calibrated following the ASTM standard.[2-4] **a** The black tape and specimen are placed on a copper tape attached to a hot plate. The top surface temperatures are recorded using an infrared camera.[2-4] **b** The emissivity of the graphite-coated SMPC and Ni plate as a function of temperature.

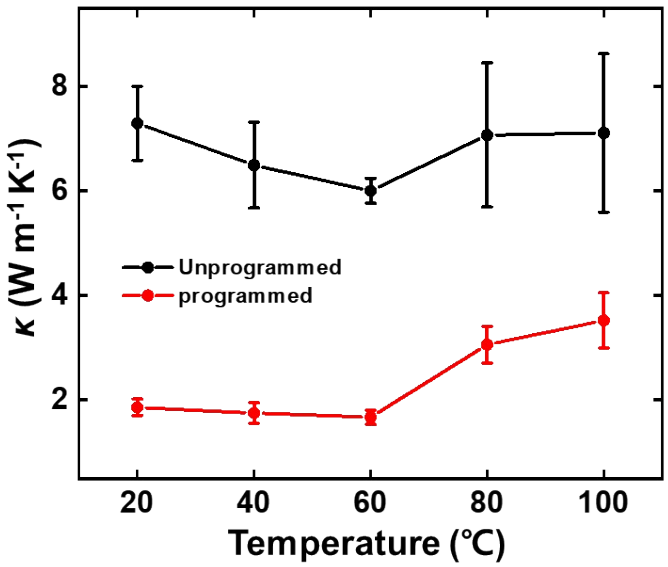

Supplementary Fig. 9 The thermal conductivity of the unprogrammed and programmed SMPC specimens as a function of temperature. The data for the programmed SMPC are reproduced from Fig. 2e for comparison.

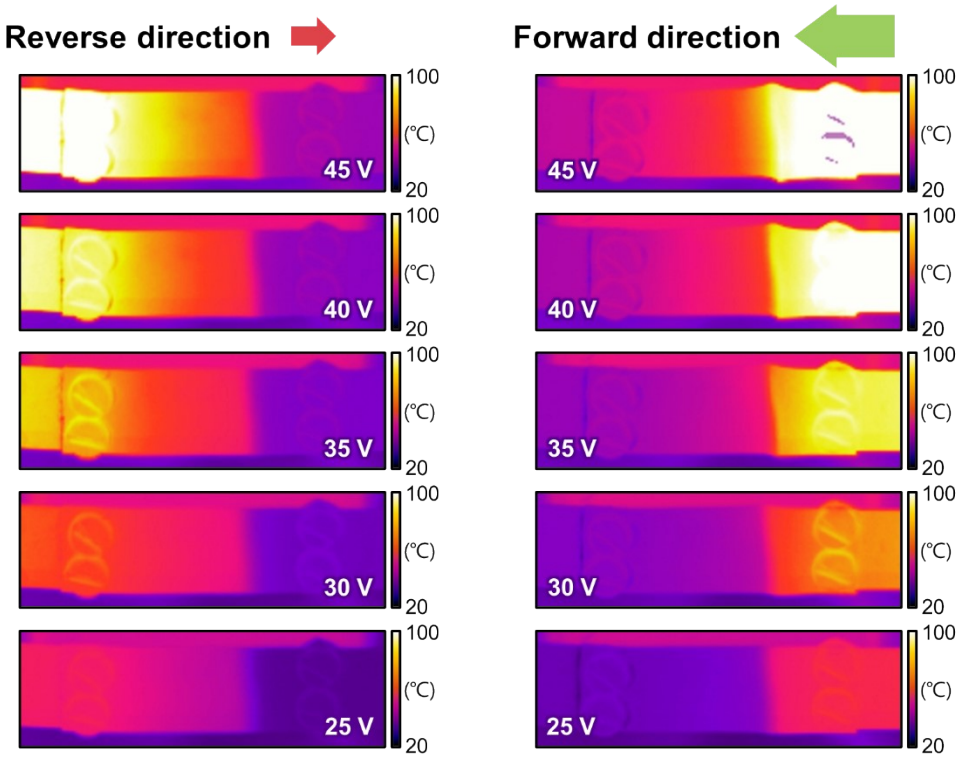

Supplementary Fig. 10 The infrared camera images of the SMPC during the reverse and forward heat flow experiments.

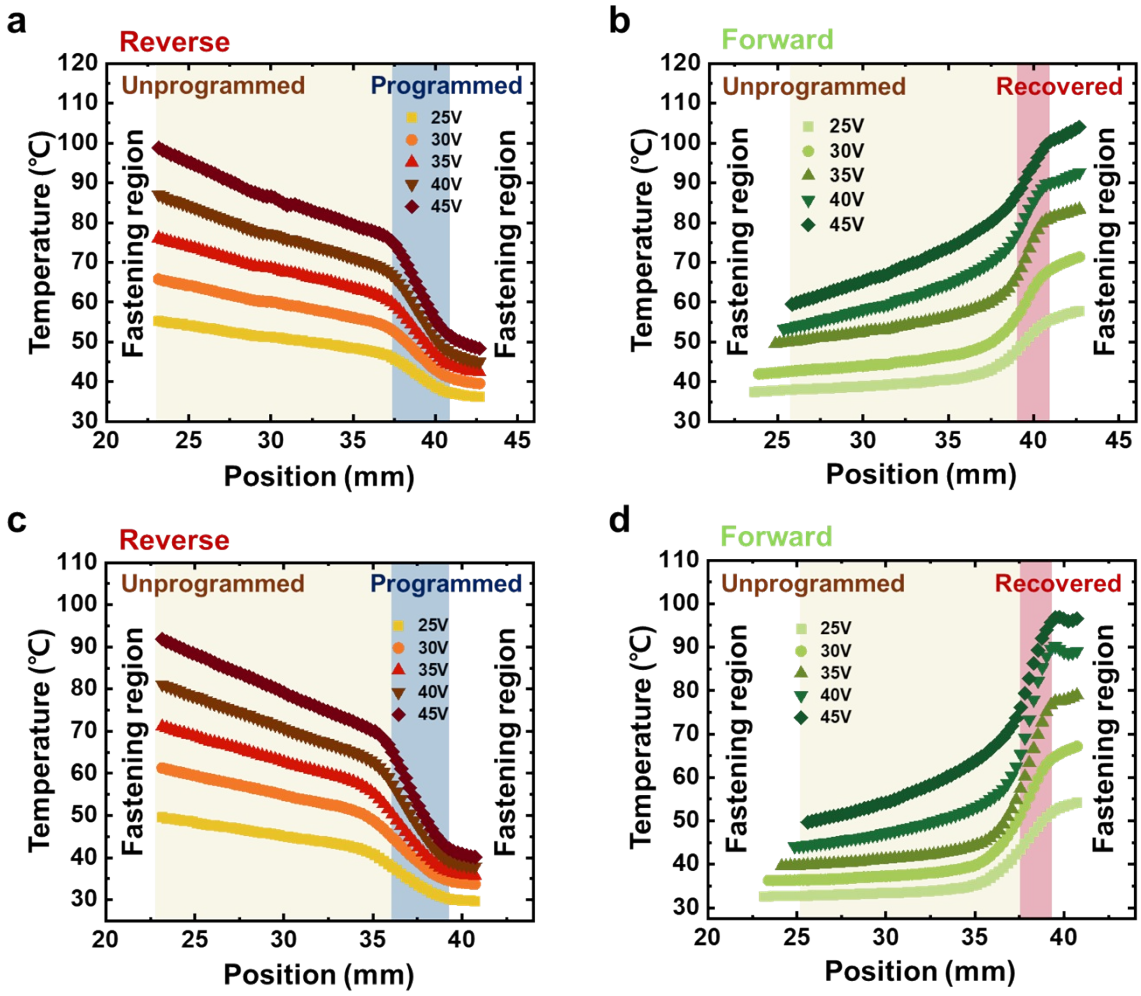

Supplementary Fig. 11 The temperature profiles of 2 additional SMPC specimens during the reverse and forward heat flow experiments. a, **b** The 2nd SMPC specimen. **c, d** The 3rd SMPC specimen.

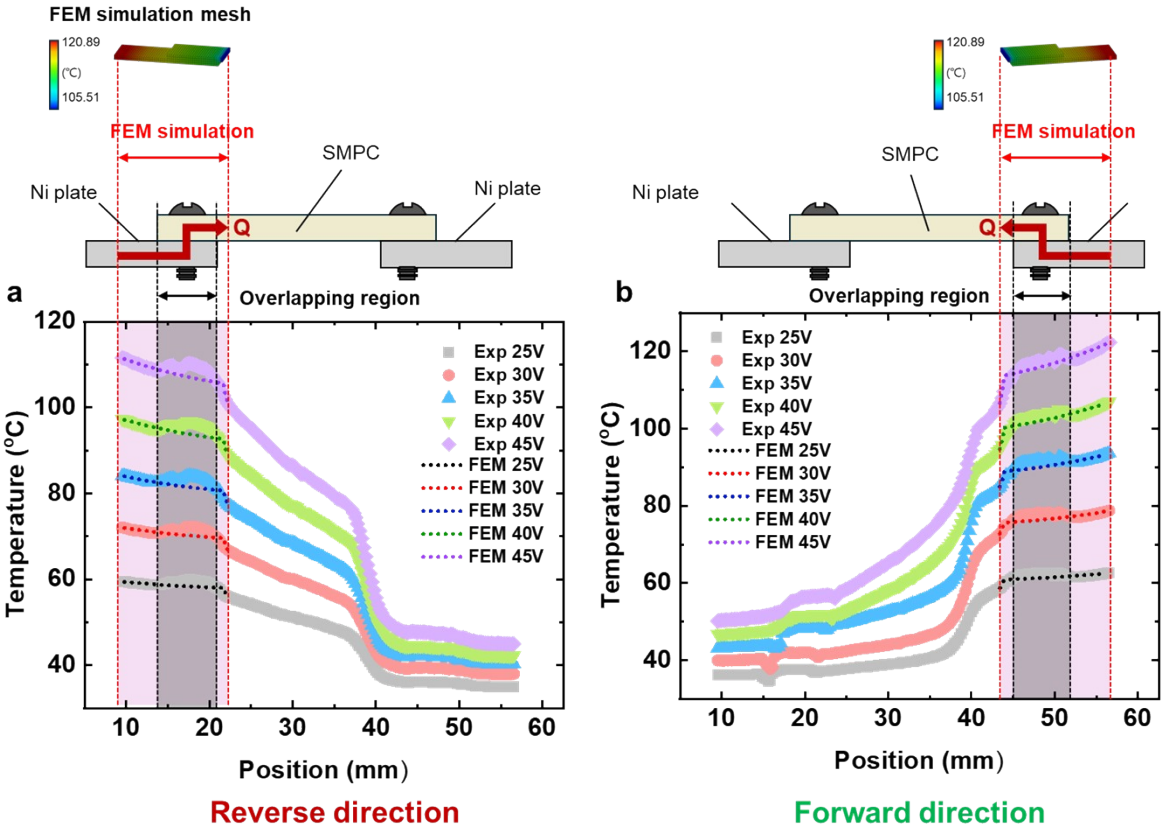

Supplementary Fig. 12 The comparison of the experimentally measured temperature profile and FEM analysis. Only the fastening region (shaded in purple) is simulated by FEM (Ansys Fluent) to calculate the input heat flow rate to the SMPC. The schematic of the experimental setup and FEM simulation mesh are also provided. The experimentally measured temperature-dependent thermal conductivity and emissivity of the nickel plate and SMPC are used for the simulation. For simplicity, the fastening bolt is not considered in the simulation. There is an excellent agreement between the simulation results and experimental data except for the fastening bolt (shaded in grey). The experimentally measured temperature of the fastening bolt shows irregular variation due to the protruded geometry and out-of-focus problem during the infrared camera measurement, in addition to the different thermal conductivity of the bolt. **a** Reverse heat flow direction. **b** Forward heat flow direction.

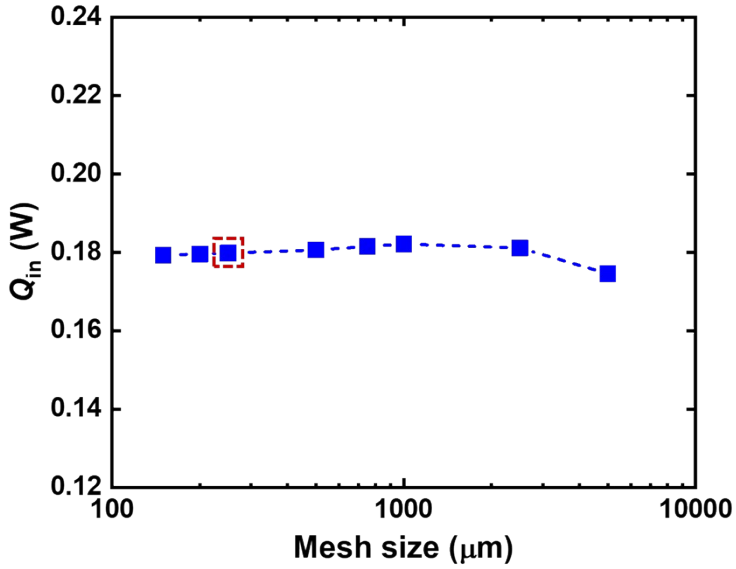

Supplementary Fig. 13 The FEM mesh convergence analysis. The heating voltage is 45 V (forward direction).

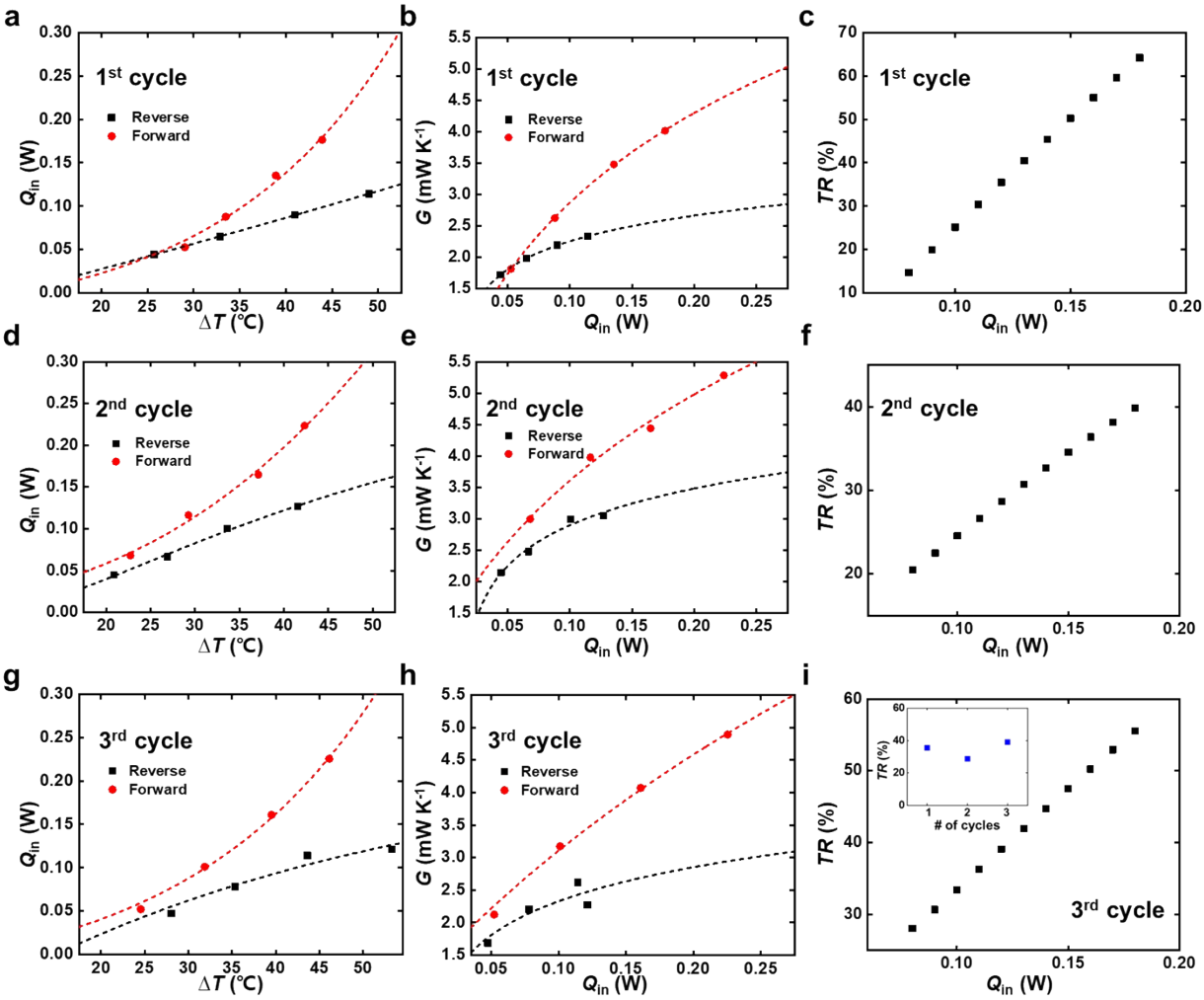

Supplementary Fig. 14 Thermal rectification behavior during cyclic testing of the SMPC. a The input heat transfer rate (Q_{in}) is shown as a function of the temperature difference between two ends of the SMPC (ΔT). **b** The thermal conductance (G) is shown as a function of Q_{in}. **c** The thermal rectification efficiency (TR) is shown as a function of Q_{in}. The TR is calculated using the regression data. **d–f** Thermal rectification behavior during the second cycle. **g–i** Thermal rectification behavior during the third cycle. The TR is also shown as a function of thermal rectification cycles (inset, Q_{in} = 0.12 W).

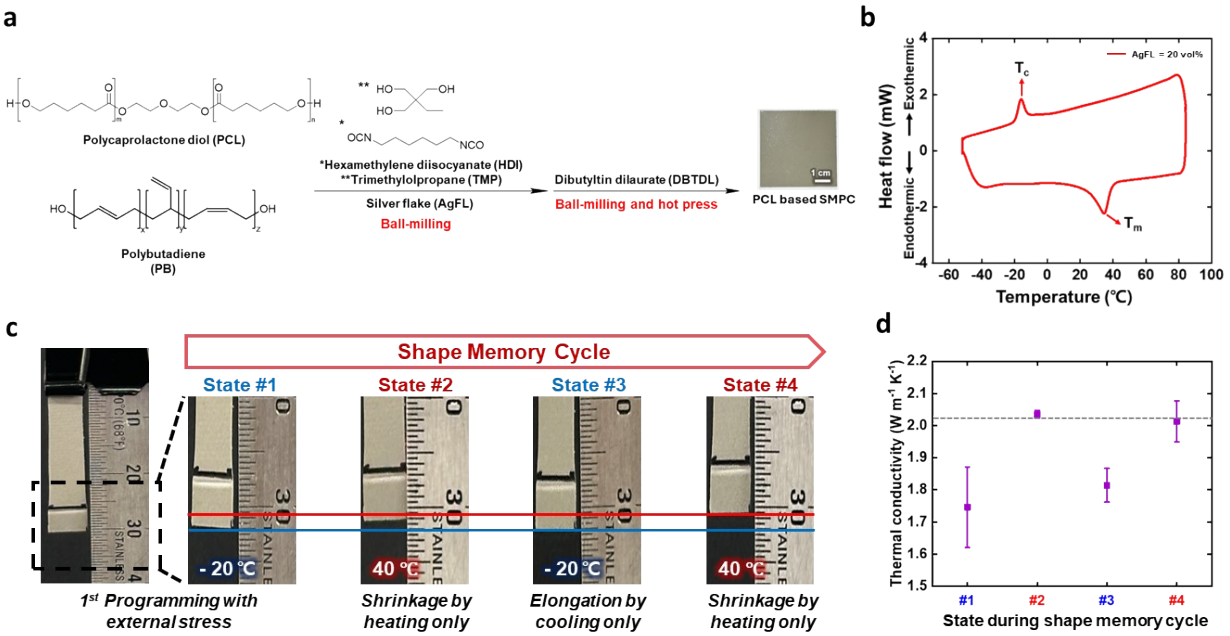

Supplementary Fig. 15 The SMPC synthesized using polycaprolactone diol and polybutadiene diol. a Schematic of the synthesis process.[5, 6] The polycaprolactone diol (PCL; Thermo Fisher Scientific, 2000 g mol^{-1}) and trimethylolpropane (TMP; Tokyo Chemical Industry Co. Ltd.) are pretreated under vacuum at 70 °C overnight to remove residual moisture. In the next step, PCL (2.0 g, 1.0 mmol), polybutadiene diol (PB; Scientific Polymer Products Inc, 3000 g mol^{-1}, 0.25 g, 0.083 mmol), TMP (42 mg, 0.31 mmol), and silver flakes (4.51 g, 20 vol% relative to the total volume of diols) are placed in a stainless steel jar (25 ml) with two stainless steel balls (15 mm). Hexamethylene diisocyanate (HDI; Tokyo Chemical Industry Co. Ltd., 0.26 g, 1.6 mmol) is then added. The reactants are homogenized using a mixer mill (30 Hz, 15 min). After mixing, dibutyltin dilaurate (DBTDL; Tokyo Chemical Industry Co. Ltd., 8 mg, 0.16 mmol) is quickly added. The prepolymer is then synthesized by further mixing at 30 Hz for 10 min. The resulting prepolymer is placed in a square stainless-steel mold (50 × 50 × 0.5 mm^3) and hot-pressed at 10 MPa and 60 °C for 4 hours. The film is demolded after cooling down to room temperature. **b** DSC analysis of the SMPC. **c** The length modulation of the SMPC during the shape memory cycle between -20 and 40 °C. The SMPC is firstly programmed by heating above the melting temperature (40 °C), stretching under external stress, and cooling to -20 °C (below T_c) while maintaining the stretched state to allow crystallization. The external stress is then released, and the specimen is reheated to 40 °C and cooled down to -20 °C again (state #1). The specimen shrinks towards the initial length when heated to 40 °C (state #2). The SMPC is elongated again, without applying external stress, when cooled down to -20 °C (state #3). It shrinks

again when heated to 40 °C (state #4). All the images are taken at room temperature. The external stress is applied during the 1st programming process only. The SMPC shows reversible length modulation by temperature variation only, without applying external stress, in the subsequent shape memory cycles. **d** The corresponding κ modulation of the SMPC at states #1-4 during the shape memory cycle.

Supplementary Table 1 Thermodynamic properties of the SMPC, with and without cross-linker, characterized by DSC analysis.[7]

Weight fraction of cross-linker (dicumyl peroxide) [wt %]	Melting temperature T_m [°C]	Crystallization temperature T_c [°C]	Enthalpy of fusion ΔH_m [J g^{-1}]	Crystallinity X_c [%]
0	85.15	68.19	13.69	31
5	75.12	56.03	9.47	27

Supplementary Note 1 The effective medium theory (Bruggeman's model).

The effective medium theory provides a theoretical framework to estimate the overall transport property of composites by averaging the physical properties of components.[8] It assumes that all components are embedded in an equivalent mean field, and the composite is treated as a homogeneous medium with an effective thermal conductivity (κ_{eff}). The Bruggeman's model treats both the matrix and filler phases symmetrically within the same effective medium.[8] For flake-type fillers, the Bruggeman model is given by:

$$V_f \frac{\kappa_f - \kappa_{eff}}{\kappa_f + \kappa_{eff}} + (1 - V_f) \frac{\kappa_m - \kappa_{eff}}{\kappa_m + \kappa_{eff}} = 0$$

where V_f, κ_m, and κ_f are the volumetric filler fraction, matrix thermal conductivity, and filler thermal conductivity. The κ_{eff} becomes 0.42 W m^{-1} K^{-1} at V_f = 17 vol%, where κ_f = 429 W m^{-1} K^{-1} (silver) and κ_m = 0.28 W m^{-1} K^{-1} (PEVA matrix).

Supplementary References

1. S. Bae and S. Baik, *Sensors and Actuators A: Physical*, 2024, **372**, 115343.
2. S. Kim, T. Kim, J. Sung, Y. Kim, D. Lee and S. Baik, *Materials Horizons*, 2023, **10**, 5720-5728.
3. ASTM E1862, Standard Practice for Measuring and Compensating for Reflected Temperature Using Infrared Imaging Radiometers (American Society for Testing and Materials International, West Conshohocken, 2018).
4. ASTM E1933, Standard Practice for Measuring and Compensating for Emissivity Using Infrared Imaging Radiometers (American Society for Testing and Materials International, West Conshohocken, 2018).
5. Y. Guo, Y. Chen, Q. Yu, H. Liu, H. Li and Y. Yu, *Chemical Engineering Journal*, 2023, **470**, 144212.
6. H. Kim, I. Cha, Y. Yoon, B. J. Cha, J. Yang, Y. D. Kim and C. Song, *ACS Sustainable Chemistry & Engineering*, 2021, **9**, 6952-6961.
7. L. Ma, J. Zhao, X. Wang, M. Chen, Y. Liang, Z. Wang, Z. Yu and R. C. Hedden, *Polymer*, 2015, **56**, 490-497.
8. C. Granqvist and O. Hunderi, *Physical Review B*, 1978, **18**, 1554.